Reliability and Failure Analysis of Lead-Free Solder Joints

Michael Meilunas and Anthony Primavera, Ph.D.
Universal Instruments Corporation
Binghamton, New York

Steven O. Dunford
Nokia Mobile Phones
Irving, Texas

Abstract
This paper provides a comparison of the air-to-air thermal cyclic reliability and associated failure modes of second level interconnects in lead-free, 1.27 mm pitch, 256 I/O BGA devices with eutectic tin-lead assemblies. Both electroless nickel/immersion gold (ENIG) and copper OSP test board surface finishes were included in this study. The assemblies were subjected to two different $0/100^{o}C$ accelerated thermal test conditions. Solder joint failures were determined with in-situ event detection and verified by resistance measurements, x-ray, cross-sectioning and dye penetration. Elemental analysis was performed on selected failed solder joints. The results of the experiment indicate that the average solder fatigue life of the lead-free alloys investigated was higher than that of the tin-lead solder. However, the fundamental crack propagation behavior of the lead-free alloys was not the same as the tin-lead samples. Failure analysis revealed that intermetallic formation, fatigue crack characteristics, and solder fatigue propagation mechanisms associated with the lead-free alloys were not common to the tin-lead samples. In addition, lead-free solder joints evaluated in rigorous failure analysis show unique features such as stress voids, crack path redirection around intermetallic formations, vertical cracking and spalling of portions of the solder joint, which are not common in traditional tin-lead BGA solder joints.

Introduction

The current transition from lead-based solder alloys to "green" alloys has been approached with caution, primarily from cost and reliability standpoints. This paper is focused on the thermal fatigue resistance and failure analysis of three lead-free alloys: 96.5Sn/3.5Ag, 95.5Sn/3.8Ag/0.7Cu and 95.2Sn/2.5Ag/0.8Cu/0.5Sb with comparisons made to eutectic 63Sn/37Pb solder. In order to properly evaluate the alloys, identical component carrier substrates for a generic BGA device were acquired. The substrates were bumped in-house by printing flux and pre-formed 0.762 mm (30.0 mil) diameter solder spheres. The bumped packages were apportioned to two separate assembly and test groups (TG1 and TG2) to provide separate validation of results. The components were assembled to ENIG and copper OSP printed circuit boards (PCB) supplied by a single manufacturer. The assembled boards were subjected to a $0/100^{o}C$ thermal cycle until failure. Lifetime and failure analysis were completed for each test group and compared.

Component and Test Board Design

A non-bumped, daisy chained, 1.27 mm pitch, 256 I/O BGA package was used for the study. The package was a specially designed test vehicle with a 28x28 mm body and a 20x20 array of solder balls depopulated to four perimeter rows. The package contained a 25.4x25.4x1.0 mm glass die that was attached to a 0.406 mm thick FR4 based substrate with a 0.075mm thick layer of underfill. The package attachment pads were solder mask defined (SMD) with an exposed diameter of 0.5842 mm and an ENIG surface finish. The packages were bumped with 0.762 mm diameter solder spheres. The solder spheres were attached by printing flux and then placing pre-formed solder spheres. The bumped substrates were reflowed in a nitrogen atmosphere. Table 1 summarizes the melting temperatures of the four solder alloys used to construct the packages.

Table 1 – Solder Melting Temperatures

Solder Alloy	Melting Temperature (^{o}C)
63Sn/37Pb	183
96.5Sn/3.5Ag	221
95.5Sn/3.8Ag/0.7Cu	217-218
95.2Sn/2.5Ag/0.8Cu/0.5Sb	216

The components were designed to produce the thermo-mechanical behavior of standard BGAs while reducing the overall complexity of the system. The three layer construction (glass die – underfill – substrate) results in a simple, homogeneous test vehicle. The large glass die extends across the entire bump array creating a package with a global CTE (coefficient of thermal expansion). The XY-direction CTE of six samples was found to be approximately 14 ppm/^{o}C as measured by Moiré interferometry. The underfill material used was selected based on its adhesive properties and glass transition temperature (~$160^{o}C$). Figure 1 provides a cross-sectional diagram of the component.

Figure 1 – Diagram of BGA Cross-Section

The assembly test boards were 1.524 mm thick multi-layered panels that utilized a tetrafunctional FR-4 core with minimum nominal glass transition temperature of 175°C. Eight BGA components were assembled to the topside of each board. The eight sites, or coupons, corresponding to the BGAs are routed such that an individual BGA assembly may be removed from the test board without interrupting the I/Os of the other components. Solder mask protected traces are located on the surface of the test board and connect each BGA site to a gold edge finger connector that is utilized to interface to an event detector. Additional traces run from the various points within the coupon daisy chain to exposed probe pads located around the perimeter of the footprint. These probe pads were included to facilitate testing by isolating the solder joints within the assembly to sets of two or three bumps. The coupons share a common ground return. Non-solder mask defined (NSMD) pad sizes of 0.508, 0.5588 and 0.6096 mm diameters are incorporated into the PCB design. The pads are approximately 0.0559 mm thick. The test boards were supplied with copper OSP and ENIG finishes. Figure 2 shows the daisy-chain of a completed assembly.
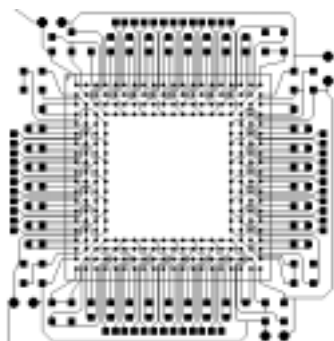

Figure 2 – Completed Daisy-Chain

Test Vehicle Assembly
The packages were baked for a minimum of 12 hours at 125°C prior to assembly in order to prevent moisture related damage during reflow operations. Assembly to the test boards was performed by stencil printing type III or IV no-clean pastes onto the PCBs. The pastes chosen for the experiment were supplied by a single vendor and utilized one flux chemistry. Paste alloy compositions were identical to the solder bump compositions. A single 0.125 mm thick stainless steel stencil was used for all assemblies. The stencil consisted of square, tapered apertures whose bottom side lengths and widths were equal to the diameters of the corresponding PCB pads. This design feature increased the paste volume deposited over the larger PCB pads and was intended to minimize standoff variation among the assemblies.

Each assembly group developed unique ramp-soak-ramp style reflow profiles for the tin-lead and the lead-free test vehicles. Profiling was performed with thermocouples attached to the test boards beneath the packages. Profiles 1 and 2 were utilized by TG1. Test vehicles subjected to Profile 1 were reflowed above the tin-lead melting temperature of 183°C for 44 seconds, reaching a peak of 219°C before solidifying at a 2.67^{o}C/sec cooling rate. Test vehicles subjected to Profile 2, a lead-free profile, were above the melting range of 216-221°C for a total of 45 seconds and reached a peak temperature of 241°C before cooling at 2.55^{o}C/sec. Profiles 3 and 4 were developed by TG2. Profile 3, a tin-lead profile, was designed to bring the assemblies above liquidus for a total of 115 seconds, reach a peak temperature of 221°C and cool at 1.3^{o}C/sec. Profile 4, a lead-free profile, resulted in a maximum temperature of 242°C followed by a 1.2^{o}C/sec cooling rate, with a total time of 46 seconds above liquidus.

Inspection
Table 2 provides the final assembly matrix. Post-reflow inspection was performed on every package. Inspection included continuity verification with a four-point ohmmeter and x-ray examination. Every assembly passed inspection. The average resistance reading for each test cell from TG1 is found in Table 3. In general, the Sn/Pb assemblies demonstrated slightly lower resistance than the lead-free assemblies. Additionally, the resistance on ENIG boards was measurably lower than the resistance on OSP boards.

Table 2 – Assembly Matrix with Sample Size

		TG1 PCB Finish		TG2 PCB Finish	
		ENIG	OSP	ENIG	OSP
Alloy	Sn/Pb	32	8	16	8
	Sn/Ag	32	8	16	8
	Sn/Ag/Cu	32	8	16	8
	Sn/Ag/Cu/Sb	40	24	8	8

Table 3 – TG1 Average Assembly Resistance (Ohms)

Alloy	Cu OSP PCB	ENIG PCB
Sn/Pb	4.865	4.829
Sn/Ag	5.389	5.245
Sn/Ag/Cu	5.331	5.146
Sn/Ag/Cu/Sb	5.218	5.036

X-ray inspection revealed that many of the Sn/Ag/Cu/Sb assemblies contained numerous voids within the solder joints. Although no voids were detected whose individual cross-sectional area exceeded 10% of the joint cross-section, several Sn/Ag/Cu/Sb joints contained a cumulative void cross-sectional area of 12-15%. Overall, the Sn/Ag/Cu/Sb voiding was more severe in samples assembled to the ENIG PCBs than those assembled to copper OSP PCBs. These findings agree with published data [1] that reports the alloy is susceptible to large voids

and void content decreases on bare copper compared to tinned pads. A typical Sn/Ag/Cu/Sb x-ray image may be found in figure 3. In general, voiding was greater in Profile 2 Sn/Ag/Cu/Sb assemblies than Profile 4 Sn/Ag/Cu/Sb assemblies. Few voids were observed among the other alloys.
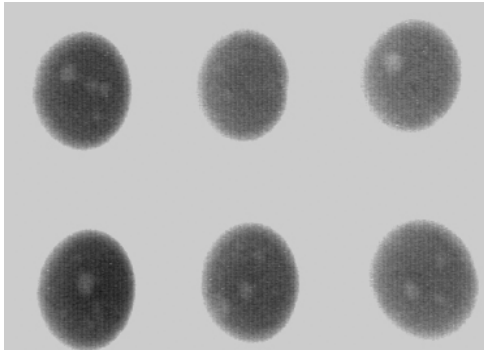

Figure 3 – Voids in Sn/Ag/Cu/Sb Solder Joints Following Assembly to ENIG PCB (Profile 2)

Accelerated Thermal Cycle
The assembled test boards were subjected to $0/100^{o}$C air-to-air thermal cycling. Table 4 summarizes the thermal cycles used by each test group. Continuous event detection was used to determine solder joint failure. Each failure was defined as a single instance of the net resistance exceeding 300 ohms for a minimum duration of 200 nanoseconds (an "event"). The IPC-SM-785 requirement of 9 additional events necessary to confirm a failure was excluded based on previous research by the author [2] that determined intermittent events associated with the lead-free alloys were indeed failures and not electrical noise. Intermittent failures in Sn/Ag assemblies have since been reported by [3] and in other lead-free assemblies by [4].

Failed components were removed from the thermal chamber following identification of electrical events. TG1 testing was terminated at 18,000 thermal cycles. Randomly chosen non-failed components were cross-sectioned or dye tested to evaluate crack propagation. TG2 testing was still in progress as of this writing.

Table 4 – Thermal Cycles Used

Test Group	Dwell Time (minutes)	Ramp Times (minutes)	Ramp Rate (^{o}C/min)
TG1	5	5	20
TG2	5	10	10

Early Failures – TG1
Twelve "early" failures were detected by TG1 in the 20 minute thermal cycle between 1576 and 5491 cycles. One failure occurred within the Sn/Ag/Cu on ENIG set, five within the Sn/Ag on OSP sample set, and three from each of the Sn/Ag/Cu/Sb on OSP and ENIG samples. Every failure was isolated by four-point probe and cross-sectioning was performed to examine the solder joints.

The Sn/Ag/Cu failure, which occurred at 2465 cycles, was the result of poor wetting and a separation between the electroless nickel plating on the package and the Sn-Ni intermetallic layer, as shown in figure 4. No other joint in the component appeared fractured. The next Sn/Ag/Cu failure occurred at 7598 cycles and regularly thereafter. The first failure, not being representative of solder performance (i.e. non-fatigue), was excluded from Lifetime analysis.
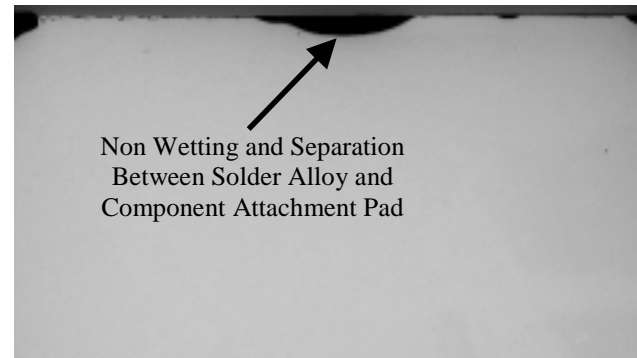

Figure 4 – First Failure of Sn/Ag/Cu Solder Joint: 2465 Cycles (20 min. cycles)

Visual inspection of five failures from the Sn/Ag/Cu/Sb sample set occurring at 1576, 1961, 3990, 3604 and 5491 cycles indicated that the glass die had delaminated from the underfill material. The delamination was possibly due to the high reflow temperatures required to assemble lead-free components. All five Sn/Ag failures (at 1534, 2262, 2452, 4140 and 4575 cycles) have also shown evidence of delamination. The effects of the delamination were evaluated by comparing delaminated samples to non-delaminated samples using Shadow-Moiré interferometry. The Moiré images show that the delaminated parts fluctuated during thermal cycling between a convex shape with the outer joints in tension to a bi-modal, or saddle shape with many of the outer joints in compression (figure 5). Non-delaminated parts fluctuated from a slightly convex shape at room temperature to a relatively flat shape at higher temperatures. The out-of-plane stress that resulted from delamination gave rise to column shaped BGA joints during reflow and lead to severe solder fracture (see figure 6) in thermal cycling. The delaminated parts were deemed package construction failures and were not used in Lifetime analysis.
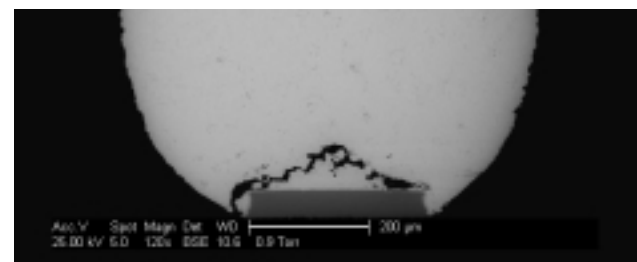

Figure 6 –First Failure of Sn/Ag/Cu/Sb Solder Joint Due to Package Delamination: 1576 Cycles (20 min. cycles)

The remaining Sn/Ag/Cu/Sb failure, which occurred at 5082 cycles was attributed to in-plane solder fatigue that had been expedited by numerous voids in the bulk solder near the package attachment pad. Figure 7 shows a failed solder joint that was affected by the presence of voids. This failure was included in Lifetime analysis because voiding was inherent to the Sn/Ag/Cu/Sb solder alloy. Failures began occurring regularly at 6150 cycles and large or numerous voids were often present in the earliest Sn/Ag/Cu/Sb failures.
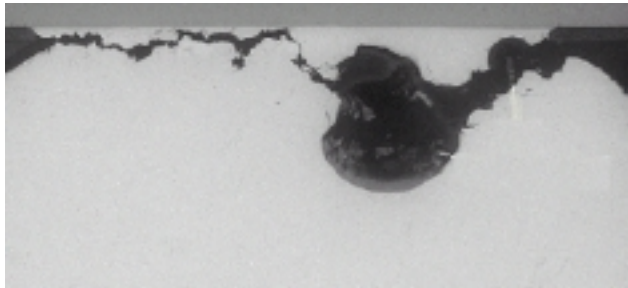
Figure 7 – Sn/Ag/Cu/Sb Failure with Voids in Crack Region: 5082 Cycles (20 min. cycles)

Early Failures – TG2
Two "early" failures were recorded by TG2 in the 30 minute thermal cycle. Both packages were Sn/Pb samples with the first failure occurring at 2959 cycles and the second failure at 3020 cycles. Analysis determined that both failures were the result of poor wetting between the electroless nickel on the BGA solder pad and the solder ball (figure 8). Sn/Pb solder fatigue failures began occurring regularly after 5885 thermal cycles.
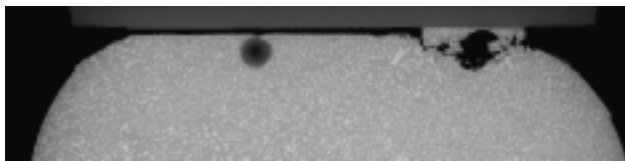

Figure 8 – Sn/Pb Solder Joint with Interfacial Failure Due to Non-Wetting: 3020 Cycles (30 min. cycles)

Lifetime Calculation
Lifetime analysis of the second level fatigue failures was performed using two-parameter Weibull distributions with median rank regression. Characteristic lifetime, or Eta, is the number of cycles at which 63.2% of the sample set has failed. The data presented in this paper has been separated into groups for each solder alloy and PCB finish combination. The effect of PCB pad diameter was evaluated separately, but no significant differences were observed. This is attributed to the use of a proportionately larger stencil aperture for the larger PCB pad assemblies that minimized solder joint standoff variation among the test vehicles. A summary of Eta values may be found in Table 5. It is important to note that the goal of this study was to determine trends among the various alloys and not to statistically qualify the lifetime of these particular component assemblies.

Table 5 – Summary of Eta Values (in Cycles)

Alloy	TG1		TG2	
	OSP	ENIG	OSP	ENIG
Sn/Pb	9849	12715	8729	8495
Sn/Ag	NA	24702	23725	17020
Sn/Ag/Cu	22919	14606	11149	10581
Sn/Ag/Cu/Sb	16504	15182	16930	9747

Figure 9 contains a Weibull plot summarizing the data from TG1 on ENIG boards. The plot shows that the Sn/Ag alloy resulted in a characteristic lifetime, Eta, which was 78% greater than that of the Sn/Pb alloy. The Sn/Ag/Cu alloy performed approximately 15% better than the Sn/Pb, and the Sn/Ag/Cu/Sb nearly 16% better. However, simply comparing Eta values undermines the importance of the successive failure rates of each alloy, which is best described by the slope, Beta. In general, lower Beta values indicate slower failure rates or a greater time between failures. This means that it is more difficult to predict when failures will occur. Comparing the Beta values clearly shows that the Sn/Ag/Cu/Sb alloy fails at a slower rate than the other alloys. This results in a higher characteristic lifetime than the Sn/Pb and Sn/Ag/Cu alloys, but also means that the probability for an early failure is increased as demonstrated by the first five fatigue failures occurring in the Sn/Ag/Cu/Sb sample set. It is believed that the presence of voids randomly located in the Sn/Ag/Cu/Sb solder arrays may have led to many of the ENIG sample set's earliest failures and low successive failure rate.

Figure 10 contains a Weibull plot of the data accumulated by TG1 on copper OSP boards. The dashed line is the predicted Sn/Ag/Cu plot based on zero failures through 16700 cycles and assuming a Beta of 6.57 (the average Beta value of the Sn/Pb and Sn/Ag/Cu/Sb sample sets) and a confidence level of –63.2%. The Weibull plot contains three distinct trend lines with the Sn/Ag/Cu/Sb Eta value 68% greater than the Sn/Pb Eta value and the Sn/Ag/Cu Eta 133% greater than the Sn/Pb Eta. No plot is provided for the Sn/Ag sample set due to the high number of delamination failures discussed earlier in the paper. The two fatigue failures of Sn/Ag on OSP boards were recorded at 9533 and 10271 cycles.

TG2 reliability data on ENIG boards is found in the Weibull plot of figure 11. As with the TG1 ENIG data, the Sn/Ag alloy has the highest characteristic life with an Eta value of 17020 cycles. The Sn/Ag characteristic life found by TG2 was twice as long as the Sn/Pb alloy. First failure for this alloy occurred at 6945 cycles with four additional failures having been detected through 16000 cycles. The Sn/Ag/Cu alloy demonstrated a lifetime of 10581 cycles, or 25% greater than the Sn/Pb with first failure occurring at 7356 cycles. The Sn/Ag/Cu/Sb alloy had a characteristic life approximately 15% greater than

the Sn/Pb with first failure at 7713 cycles and a lifetime of 9747 cycles.

Figure 12 contains a two parameter Weibull plot of all the component fatigue failures from TG2 on copper OSP PCBs. For TG2, the three lead-free alloys were found to have significantly higher characteristic lives than the Sn/Pb samples. The Sn/Pb alloy BGA samples has an Eta of 8729 cycles with the first fatigue failure occurring at 7631 cycles and regularly thereafter. The Sn/Ag/Cu/Sb showed a characteristic life 94% higher than Sn/Pb with an Eta of 16930 and first failure at 11134 cycles. The Sn/Ag/Cu alloy had a 28% higher characteristic lifetime (11149 cycles with first failure occurring at 8051 cycles), compared to Sn/Pb samples. Similar to TG1, the Sn/Ag alloy showed the highest characteristic life with a predicted Eta of 23725 cycles. Only 2 of 8 Sn/Ag packages failed through 16700 cycles. The first TG2 Sn/Ag failure on copper OSP PCBs occurred at cycle 13521.

The data collected from both TG1 and TG2 groups indicates that, for every test cell, the Sn/Pb alloy has the lowest characteristic lifetime, Eta. In general, the Sn/Ag alloy has a significantly higher characteristic life than the other materials. Differences between the Sn/Ag/Cu and Sn/Ag/Cu/Sb alloys are less apparent. Overall, the reliability differences between the Sn/Pb and lead-free alloys are in line with previously published results [5, 6, 7, 8].

6 out of the 7 complete test cells summarized in Table 5 indicate some reliability improvement by assembling to copper OSP including all 5 lead-free test cells. The estimated improvement in characteristic life ranged from 10% to over 100% in lead-free copper OSP assembly lifetime compared to the lead-free samples assembled onto ENIG pads. It is important to recall that the component pad finish was ENIG for all samples, and the motherboard pad finish was varied between ENIG and copper OSP. Reliability differences were most dramatic in the TG1 Sn/Ag/Cu and TG2 Sn/Ag and Sn/Ag/Cu/Sb assemblies. In fact, no failures have been detected in the TG2 Sn/Ag and Sn/Ag/Cu/Sb on copper OSP samples through 13,700 cycles. However, a majority of the samples failed from the same alloy sets on ENIG pad finishes.

Comparing the cycles to failure data between the 20 minute (TG1) and 30 minute (TG2) tests indicates that the reliability of the Sn/Ag/Cu alloy is more sensitive to the thermal cycle test conditions than the other alloys. A recent study [5] confirms that the Sn/Ag/Cu alloy's fatigue behavior on copper OSP PCBs is highly sensitive to the thermal cycle conditions and showed that an increased cycle time minimizes the reliability differences between the Sn/Pb and Sn/Ag/Cu.

Lifetime Comparison to Companion Study

The reliability results of TG1 and TG2 were compared to those of a companion study conducted at Nokia Mobile Phones in Irving, Texas [9]. The companion study utilized identical PCBs and components, but incorporated different pastes, reflow parameters and a –40/125°C thermal cycle. The reliability results for the Sn/Pb, Sn/Ag and Sn/Ag/Cu alloys on OSP and ENIG PCBs are summarized by the Weibull plots of figures 13 and 14.

As with the previous Weibull plots, non-fatigue failures have been removed as have early failures that significantly increase the Beta value and improperly improve the characteristic life. These failures included many interfacial failures between the ENIG component finish and solder alloy. Similar to the TG1 and TG2 data, the lead-free alloys show a reliability improvement when assembled to copper OSP. The results indicate that, for this thermal cycle (and reflow conditions), the Sn/Ag/Cu alloy demonstrates the greatest reliability regardless of surface finish. The Sn/Ag alloy outperforms Sn/Pb on copper OSP assemblies, but fared poorly on ENIG finish. The reasons for such differences are not clearly understood, it is believed that the Sn/Ag alloy was negatively impacted by intermetallic and grain boundary formations which reiterates the importance of reflow profile and thermal cycle parameters on the reliability of lead-free alloys. For more details concerning the companion studies refer to [9].

Failure Analysis
Nearly 85% of the test vehicles were subjected to post-thermal cycle analysis. All samples were x-rayed and many of the specimens, including the earliest failures discussed previously, were cross-sectioned to the failure location as determined by 4-point continuity verification. Note that cross-sectioning was not necessarily performed through the mid-plane of the solder joints because many of the packages were not electrically open, but rather demonstrated resistance increases from their initial state. Dye penetration analysis was used to compile statistical data on which joint locations, if any, were most susceptible to failure.

Sn/Pb Failures
100% of the Sn/Pb failures from both TG1 and TG2 evaluated contained fractured solder joints. Figure 15 shows a Sn/Pb solder joint on an ENIG PCB that failed at cycle 6801. This joint was fatigued through the bulk solder material located in the solder mask defined region of the joint near the component body. The crack path is well defined and clearly visible under microscopic examination. Nearly identical results were obtained for all the Sn/Pb samples; bulk solder fatigue in the SMD region of the joints.
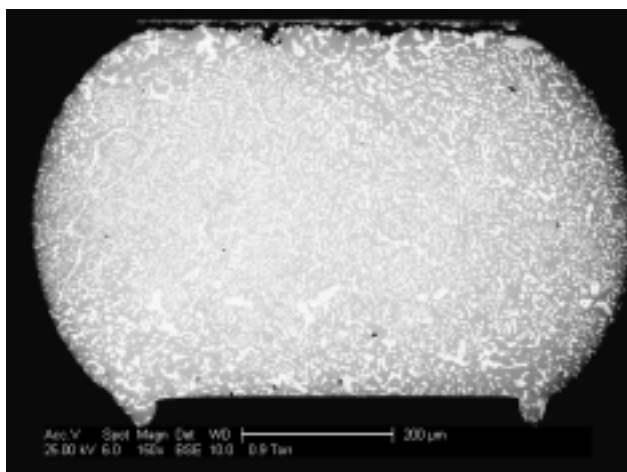
Figure 15 – Failed Sn/Pb Solder Joint after 6801 Cycles (20 min. cycles)

The final TG1 Sn/Pb failure occurred at cycle 16698. Although the package was electrically open, one joint that was electrically good contained a vertical crack visible on the surface of the joint as shown in figure 16. The crack appears to coincide with the grain boundary that has formed during temperature cycling. No such crack was observed in any other Sn/Pb component.
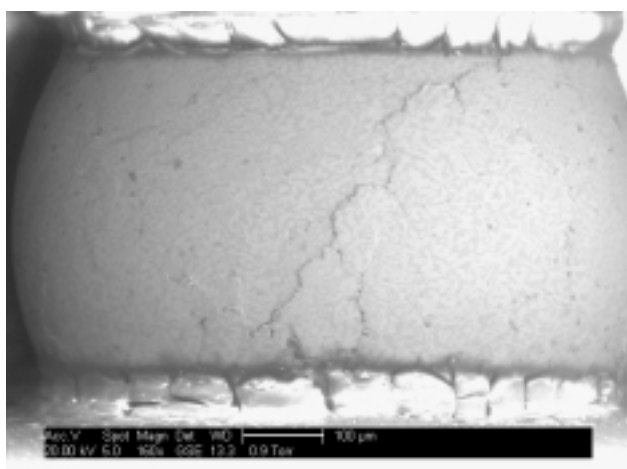

Figure 16 – Electrically Good Sn/Pb Solder Joint after 16698 Cycles (20 min. cycles)

Lead-Free Failures
Analysis of the lead-free failures revealed not only a variety of failure modes, but also many interesting and potentially important issues associated with the alloys. Most noticeable was the existence of two distinct fracture paths: well defined cracks similar to that observed in Sn/Pb failures and fine microcracks that were often difficult to detect without the aid of SEM. The differences become clear when comparing figures 17 and 18. Figure 17 is that of a Sn/Ag/Cu solder joint following 10885 thermal cycles. A single, wide fracture surface extends across the solder joint in the SMD region near the component. The crack path is fairly straight and remains in the bulk solder just below the intermetallic region. Cracks of this nature were easily located by 4-point

continuity measurements. Figure 18 is that of a Sn/Ag/Cu solder joint after 7598 cycles. A very fine crack with multiple fronts has propagated through the joint, resulting in a "shattered" appearance. Portions of the crack are located in the bulk solder while other portions have propagated into the intermetallic region. The formation, location and propagation of microcracks in Sn/Ag alloys in and near the intermetallic region has been noted in other works [10, 11]. The "shattered" cracks of this experiment were often difficult to isolate with a 4-point meter, and required careful comparisons between pre- and post-cycle resistance measurements to locate. Additionally, the event detector output corresponding to assemblies containing microcracks was often similar to output associated with noise or intermittent failure. The event detection criteria was based on IPC SM-785, with a 300 Ohm resistance level and a 200 nanosecond time duration. However, resistance changes as small as 5-25 Ohms for a 40 nanosecond duration were measured with a more sensitive event detection system in certain lead-free samples during thermal cycling. These small resistance levels were confirmed to coincide with crack propagation. Thus selection of low resistance thresholds may be required for testing of lead-free solder compared to eutectic Sn/Pb solder.
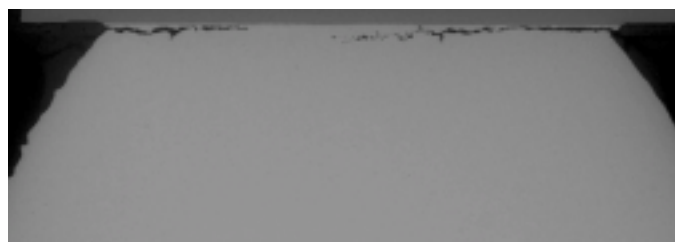

Figure 17 – Failed Sn/Ag/Cu Solder Joint after 10885 Cycles (20 min. cycles)
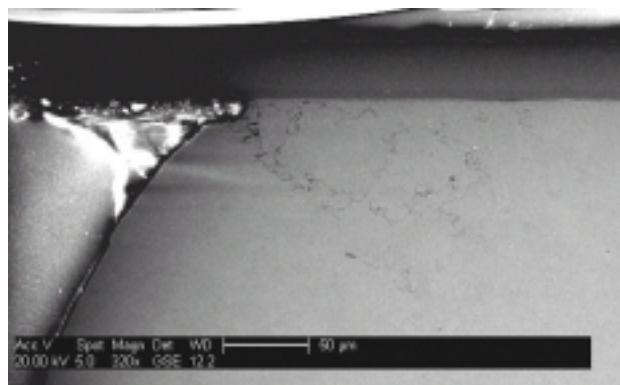

Figure 18 – Failed Sn/Ag/Cu Solder Joint after 7598 Cycles (20 min. cycles)

Generally, the wide, single path style cracks were observed near the component body in the SMD region of the joints. However, the "shattered" cracks were just as likely to occur near the PCB pad as they were near the component pad. Figure 19 shows the region of a Sn/Ag solder joint on a Cu OSP PCB pad. The crack has

propagated around the NSMD PCB pad through the bulk solder. No correlation between cycles to failure and the "shattered" crack locations (component side vs. PCB side) was observed. No correlation between crack type and cycles to failure was observed.
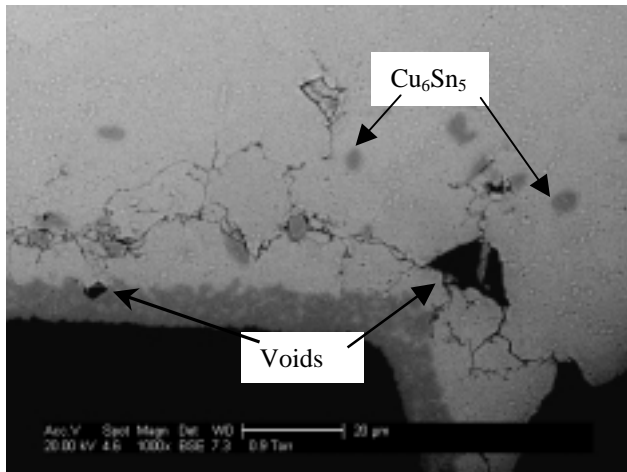

Figure 19 – Failed Sn/Ag Solder Joint on Cu Pad after 10204 Cycles (20 min. cycles)

Vertical cracking, similar to that seen in the Sn/Pb sample of figure 16, was observed in several lead-free failures (figure 20). The joints were electrically good and the vertical crack was not found by event detection or 4-point measurements. However, visual inspection identified vertical cracks in many assemblies. Unlike the vertical crack found in the Sn/Pb sample, these cracks were large enough to view with x-ray, as shown in figure 21. It is supposed that these vertical cracks may lead to spalling in some of the lead-free samples before in-plane fracture is completed, thus introducing a new failure mode.
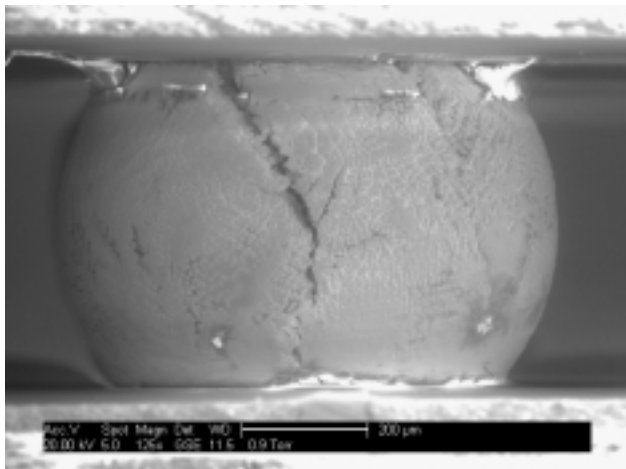
Figure 20 –Sn/Ag/Cu/Sb Solder Joint Vertical Crack after 16700 Cycles (20 min. cycles)
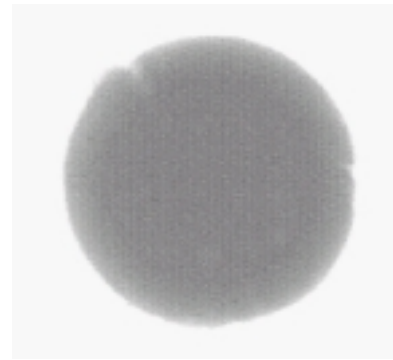

Figure 21 – Electrically Good Sn/Ag/Cu Solder Joint after 14115 Cycles (20 min. cycles)

Lead-Free Intermetallics
Cu_6Sn_5 and Ag_3Sn intermetallics were commonly observed throughout the bulk solder in both the Sn/Ag/Cu and Sn/Ag/Cu/Sb alloys. The Ag_3Sn was also present in all bulk Sn/Ag alloy but Cu_6Sn_5 could only be found near the copper PCB pads. The formation of these intermetallics has been well documented [12, 13, 14, 5] and it has been noted that such formations have the potential to strengthen the joints [15, 16]. By referring back to figure 19, one may observe the effect of intermetallics on crack path behavior. In this particular case, the crack appears to propagate around the Cu_6Sn_5 phases near the PCB pad.

Figure 19 also shows that several small voids exist in the crack region. These voids may be the result of intermetallic formation and/or internal stresses which deform the joint. The small voids were most often observed at or near the thick, continuous layer of Cu-Sn that formed between the solders and copper OSP PCBs. This intermetallic region consisted primarily of Cu_6Sn_5 although some specimens contained a very thin layer of Cu_3Sn between the copper pad and Cu_6Sn_5 intermetallic. Many papers have been published documenting the presence of the Cu-Sn intermetallic layers including [5, 17]. Measurements indicate that the post-reflow intermetallic thickness was approximately 0.0043 mm for all three lead-free alloys and grew to excess of 0.00635 mm by the onset of solder fatigue. Less Cu-Sn intermetallic was observed in the Sn/Ag/Cu and Sn/Ag/Cu/Sb on Cu OSP assemblies than was observed with the Sn/Ag, possibly due to the presence of Cu within the alloys which limited the interaction between the copper board and solder. Sn/Pb samples on copper PCBs contained both Cu_6Sn_5 and Cu_3Sn but the thickness was limited.

Intermetallic formations between the nickel plated PCB pads and lead-free solder alloys may include Ni_6Sn_5 and Ni_3Sn_4 or Cu_6Sn_5 and Cu_3Sn_4 if copper is present in the alloy [18]. The presence of Ag, Au and Cu in the solder joint will potentially cause the formation of $AuSn_4$, $Au_{0.1}Ni_{0.1}Sn_{0.8}$ [18] and $Cu_{0.1}Ni_{0.1}Sn_{0.8}$ [19, 20, 21] as well. The intermetallics encountered during this

experiment were predominantly Ni-Sn although some Cu-Sn was observed in a few Sn/Ag/Cu samples. The Ni-Sn intermetallics were characterized by a blocky, irregular shape and were in excess of 0.0040 mm thick following reflow (figure 22). The growth of Ni-Sn during thermal cycle was not as dramatic as the growth of the Cu-Sn intermetallic. The largest Ni-Sn intermetallic observed measured approximately 0.0057 mm thick after 9036 20 minute thermal cycles. The composite intermetallic layer thickness near the attachment pad has been compared to other lead-free soldered samples found in literature as presented in Table 6. The composite layers of intermetallic have been shown to grow significantly faster than Sn/Pb alloys on both copper and nickel pad surfaces.
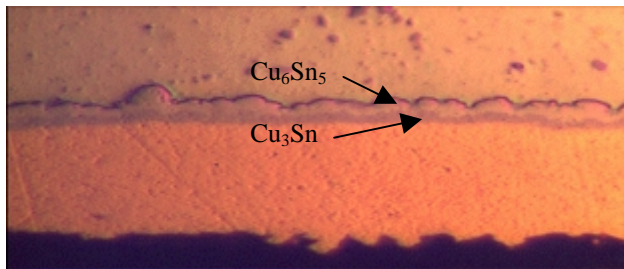
Figure 22 – Sn/Ag/Cu Solder Joint on Cu Pad Post-Reflow (Profile 2)

Figure 23 and Table 6 show the accelerated growth of the composite intermetallic layer for several lead-free solders as a function of time (thermal exposure).
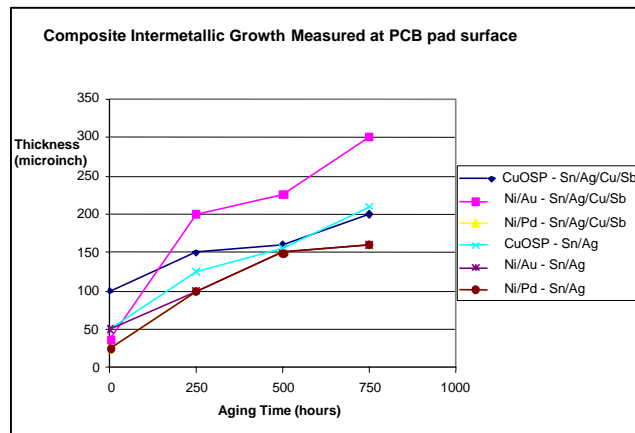

Figure 23 – Intermetallic Growth Rate

There is sufficient evidence to suggest that Cu-Sn and Ag_3Sn intermetallics may temporarily redirect cracks that typically run parallel to the component or PCB pad through the predominantly Sn matrix. Figure 24 is one of several Sn/Ag/Cu solder joints that contained large Ag_3Sn plates that formed at a 45° angle to the component pad. Instead of propagating along the pad region, the crack path runs alongside the plate towards the center of the solder joint. This increase in path length may translate into longer joint life, however plate orientation may run in any direction, even parallel to the crack path.
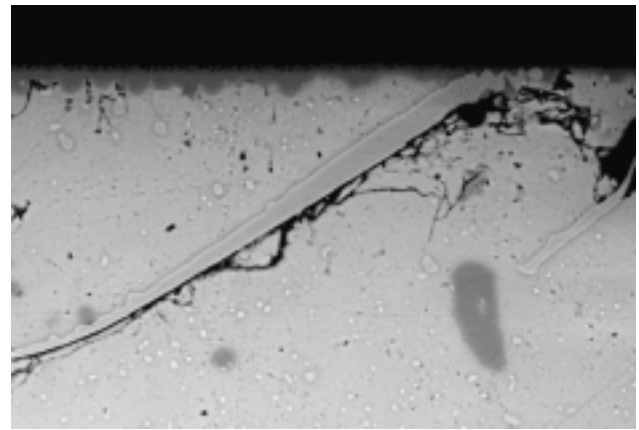

Figure 24 – Failed Sn/Ag/Cu Solder Joint after 14340 Cycles (20 min. cycles)

Stress Voiding
Another phenomenon observed in the lead-free assemblies has been termed "sinkholes". The sinkhole may be described as a long, thin void originating at the solder joint surface that appears to form during reflow and grow during thermal cycling. Sinkholes appeared to be most common in the Sn/Ag/Cu and Sn/Ag/Cu/Sb alloys. Cross-sectioning revealed one sinkhole extending approximately 0.138 mm (about 1/6th of the solder joint diameter) into a Sn/Ag/Cu/Sb solder joint (figure 25). The effects of the sinkhole on the thermal or mechanical behavior of the joints is uncertain. No failures were directly associated with sinkholes.
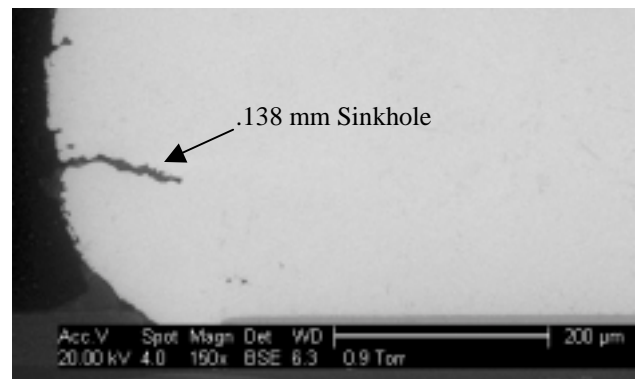

Figure 25 – Sinkhole Void Sn/Ag/Cu/Sb Solder Joint after 12500 Cycles (30 min. cycles)

Failure Frequency Plots
The BGA samples were designed to produce a homogeneous CTE. Such a design, when assembled to a PCB should stress the solder joints in direct proportion to their distance from the neutral point (DNP) during thermal cycling as described by the equation:

$$\varepsilon = (\Delta\alpha * \Delta T * DNP) / h$$

where ε is strain on a joint, $\Delta\alpha$ is the difference between the CTE of the BGA and the CTE of the PCB, ΔT is the cyclic temperature swing, and h is the solder joint height or standoff. Assuming that $\Delta\alpha$, ΔT and h are constant within an assembly, the equation shows that the corner most joints, with the greatest DNP, should be most

susceptible to fatigue damage. In order to evaluate the hypothesis, assemblies from each test cell were selected and dye penetration analysis was performed to determine which joint locations were likely to fail. Low atmospheric pressure was required for the dye to penetrate the fine cracks found in the lead-free solder joints.

The failure frequency diagrams in this paper show the number of BGA joints and their locations in the solder array where approximately 25% or more of the joint was fatigued. If the criterion is lowered below 25%, a far greater number of joints must be included in the diagrams because small cracks were located throughout the solder joint arrays. Figure 26 summarizes the results from 42 Sn/Pb BGAs, which shows that the corner regions of the packages are most likely to fail. No significant differences were observed between the ENIG and copper OSP PCB finishes.

Figure 26 – Failure Frequency of Sn/Pb BGAs (TG1 & TG2 Copper OSP and ENIG PCBs: 42 Samples)
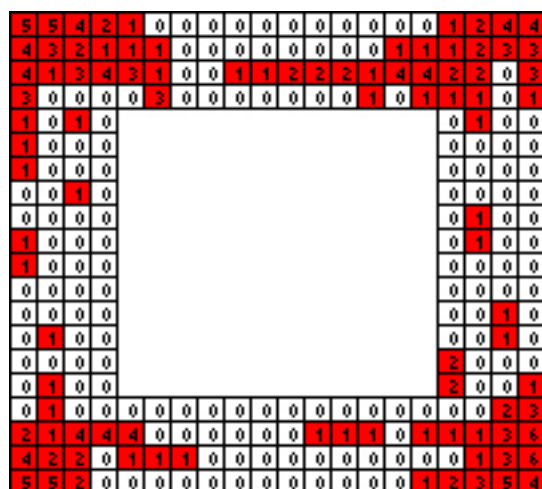
Figure 27 summarizes the results from 38 Sn/Ag/Cu BGAs. The failure locations appear to be randomly distributed throughout the solder array. There was no significant difference between failure location and PCB finish. Similar results were observed with the 33 samples of the Sn/Ag/Cu/Sb alloy (figure 28). Sn/Ag failures were subjected to dye penetration analysis and the failure frequency plot may be found in figure 29. For this alloy the corner most solder joints fail earliest in agreement with the DNP hypothesis.
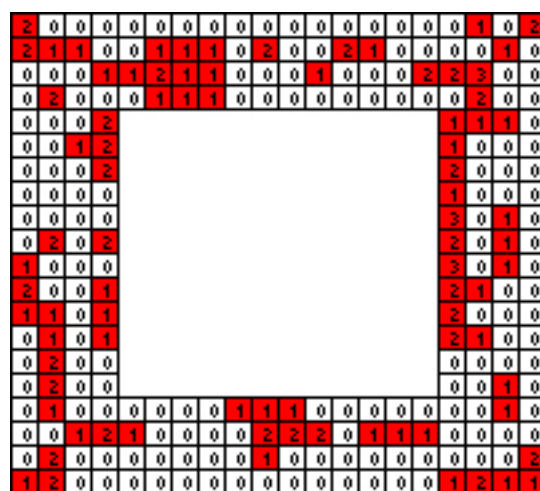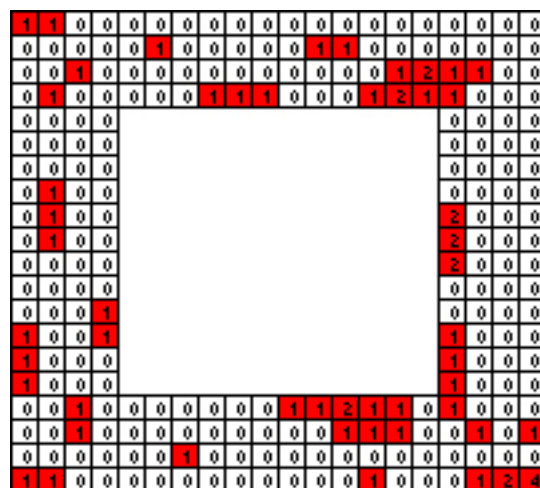
Figure 27 – Failure Frequency of Sn/Ag/Cu BGAs (TG1 & TG2 Copper OSP and ENIG PCBs: 38 Samples)

Figure 26 – Failure Frequency of Sn/Ag/Cu/Sb BGAs (TG1 & TG2 Copper OSP and ENIG PCBs: 33 Samples)
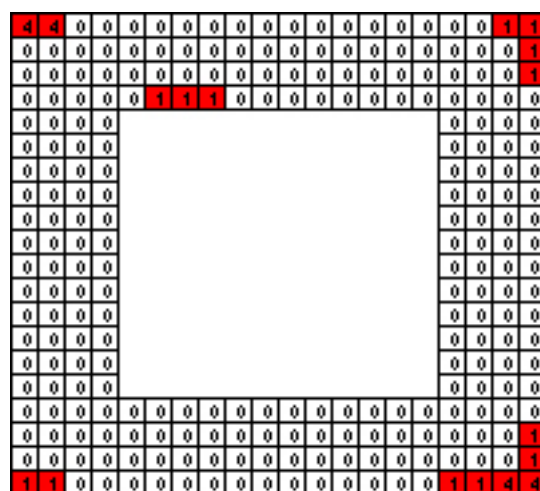
Figure 29 – Failure Frequency of Sn/Ag BGAs (TG1 & TG2 Copper OSP and ENIG PCBs: 13 Samples)

Conclusions

The data generated from TG1 and TG2 suggests that all three lead-free alloys have a greater characteristic lifetime compared to eutectic Sn/Pb in 0/100°C temperature cycling. The Sn/Ag alloy showed the highest Eta, which was twice as great as that of Sn/Pb.

Early failures were often attributed to interfacial failures between the component nickel plating and solder alloy. This failure mechanism was observed with all four alloys and was not limited to the Sn/Pb samples.

Three fatigue mechanisms were consistently observed within the lead-free systems: typical component side fatigue, multiple crack path solder fatigue, and vertical cracks. Component side fatigue was most always located in the bulk solder at the SMD region of the joint below the PCB / component interface. The fine, multiple crack path solder fatigue was observed near both the component side and PCB side of the solder joint and was often difficult to detect with 4-point resistance measurements. Vertical cracking along the surface of the solder joint can occur during thermal cycle and may lead to spalling of the solder joints.

Test criteria used in this research for event detection was a modified IPC SM-785 requirement for resistance levels. A 300 Ohm resistance level and a 200 nanosecond time duration was utilized due to the extremely sensitive nature of the lead-free samples to propagation of fine cracks. Resistance changes as small as 5-25 Ohms for a 40 nanosecond duration were measured for some of the lead-free samples during thermal cycling. Use of event detection equipment with low trigger thresholds is therefore recommended for testing of the lead-free alloys. Figure 30 shows two low resistance events recorded by an oscilloscope during a 300 second interval of a thermal cycle test.
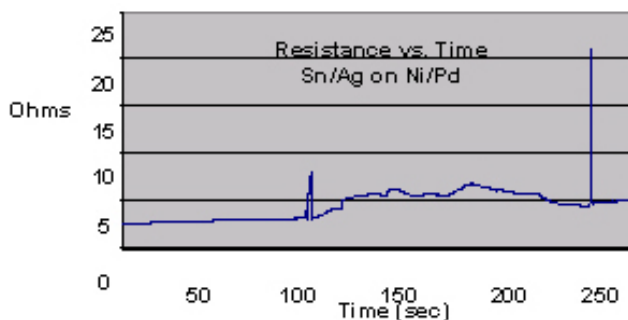

Figure 30 – Resistance Versus Time During Cycling

Intermetallic plate formation may improve the reliability of lead-free solder joints. Sn-Ag plates were observed in all three lead-free alloys and show evidence of redirecting crack propagation. Cracks were shown to propagate around Sn-Cu intermetallics present in the bulk solder of the lead-free alloys. This theory is supported in the companion paper [9].

Dye penetration analysis indicates that predicting reliability using DNP calculations may be invalid for the Sn/Ag/Cu and Sn/Ag/Cu/Sb alloys. It is believed that the randomness associated with intermetallic and grain boundary formation/orientation significantly alters the reliability of individual joints. The presence of voids in the Sn/Ag/Cu/Sb joints may also decrease the reliability of the alloy.

Lead-free solder alloys can be used in place of Sn/Pb in many applications. The reliability of Sn/Ag, Sn/Ag/Cu and Sn/Ag/Cu/Sb BGAs has been shown to be greater than that of Sn/Pb BGAs in 0/100°C thermal cycle tests. But our understanding of the materials is limited. This study has shown that lead-free failure times, failure mechanisms and failure locations are significantly different than that of Sn/Pb and more work will be required to better understand the consequences of lead-free soldering.

References

1. Raby J., et al., "New No-lead Solder Pastes and Reflow Techniques", Circuits Assembly, March 2002.
2. Meilunas, M., et al., "Resistance Monitoring of Lead-Free Solder Alloys", Universal Instruments Area Array Consortium, October 2000.
3. Mawer A., et al., "Automotive PBGA Assembly and Board Level Reliability with Lead-Free Versus Lead-Tin Interconnect", Journal of SMT, January 2001.
4. Dunford, S., *Private Communication*, 2001.
5. Bartelo, J., et al., "Thermomechanical Fatigue Behavior of Selected Lead-Free Solders", IPC SMEMA Council APEX 2001.
6. Syed, A., "Overview of Reliability Models and Data Needs", Workshop on Modeling and Data Needs for Lead-Free Solders, 2001.
7. Chalco, P., "Solder Fatigue Reliability Issues in Lead Free BGA Packages", Pan Pacific Symposium, 2002.
8. Wiese, S., et al., "Constitutive Behavior of Lead-free Solders vs. Lead Containing Solders – Experiments on Bulk Specimens and Flip-Chip Joints", Proceedings of the 2001 Electronic Components and Technology Conference, May 29 – June 1, 2001.
9. Dunford, S., Primavera, A., and Meilunas, M., "Microstructural Evolution and Damage Mechanisms

in Pb-free Solder Joints During Extended –40 to 125C Thermal Cycles. IPC 2002 New Orleans, LA, Nov 2-3, 2002

10. Igoshev, V.I., et al., "Creep Phenomena in Lead-Free Solders", Journal of Electronic Materials, Volume 29, No. 2, 2000.

11. Suganuma, K., et al., "Microstructure and Strength of Interface Between Sn-Ag Eutectic Solder and Cu", Japan Institute of Metals, C59, 1995.

12. Chada, S., et al, "Microstructural Investigation of Sn-Ag and Sn-Pb-Ag Solder Joints", Soldering and Surface Mount Technology, 1997.

13. Warwick, M., "Implementing Lead Free Soldering – European Consortium Research", Jounal of SMT, 1999.

14. Abtew, M., "Lead-Free Solders in Microelectronics", Materials Science and Engineering Reports, 2000.

15. Albrecht, et al., "A Study of Microstructural Change of Lead-Containing and Lead Free Solders", Journal of SMT, Volume 15 Issue 2, 2002.

16. Poon, N.M., et al., "Residual Shear Strength of Sn-Ag and Sn-Bi Lead-Free SMT Joints After Thermal Shock", IEEE Transactions on Advanced Packaging, Volume 2, No. 4. November 2000.

17. Kay, P.J., et al., "The Growth of Intermetallic Compounds on Common Basis Materials Coated with Tin and Tin-Lead Alloys", Transactions of the Institute of Metal Finishing, Volume 54, 1976.

18. Zribi, A., et al., "Growth of Ternary Intermetallic Alloys in Pb-Sn and Cu-Ag-Sn Pb-free Electronic Joints", Electronics Component and Technology Conference, 2001.

19. Bradley, E., and Banerji, K, "Effect of PCB Finish on the Reliability and Wettability of Ball Grid Array Packages", IEEE Transactions CPMT Part B, 1995, pp. 320-330.

20. Bradley, E., Lall, P., and Banerji, K., "Effect of Thermal Aging on the Microstructure and Reliability of Ball Grid Array (BGA) Solder Joints", SMI Proceedings, Vol. 1, 1996, pp. 95-106.

21. Gupta, K.P., Rajendraprasad, S. B., Ramakrishna, D., and Jena, A. K. ,"The Cu-Ni-Sn System", Journal of Alloy Phase Diagrams, Vol. 4., No. 3, September 1988, pp. 160-168.

22. Wild, R. N., "Properties of Some Low Melt Fusible Solder Alloys", Inter Nepcon, Brighton, England, October 19-21 1971.

23. Schetty, R., "Pb-free External Lead Finishes for Electronic Components: Tin-Bismuth and Tin-Silver", IEMT / IMC Proceedings, 1998, pp 380-385

24. Levis,K-M, and Mawer, A., "Assembly and Solder Joint Reliability of Plastic Ball Grid Array with Lead-Free Versus Lead-Tin Interconnect", ECTC 2000, pp. 1198-1204.

25. Blair, H., Pan, T-Y., and Nicholson,J., "Intermetallic Compound Growth on Ni, Au/Ni, and Pd/Ni Substrates with Sn/Pb, Sn/Ag, and Sn Solders", Electronics Component and Technology Conference, 1998, pp. 259-267.
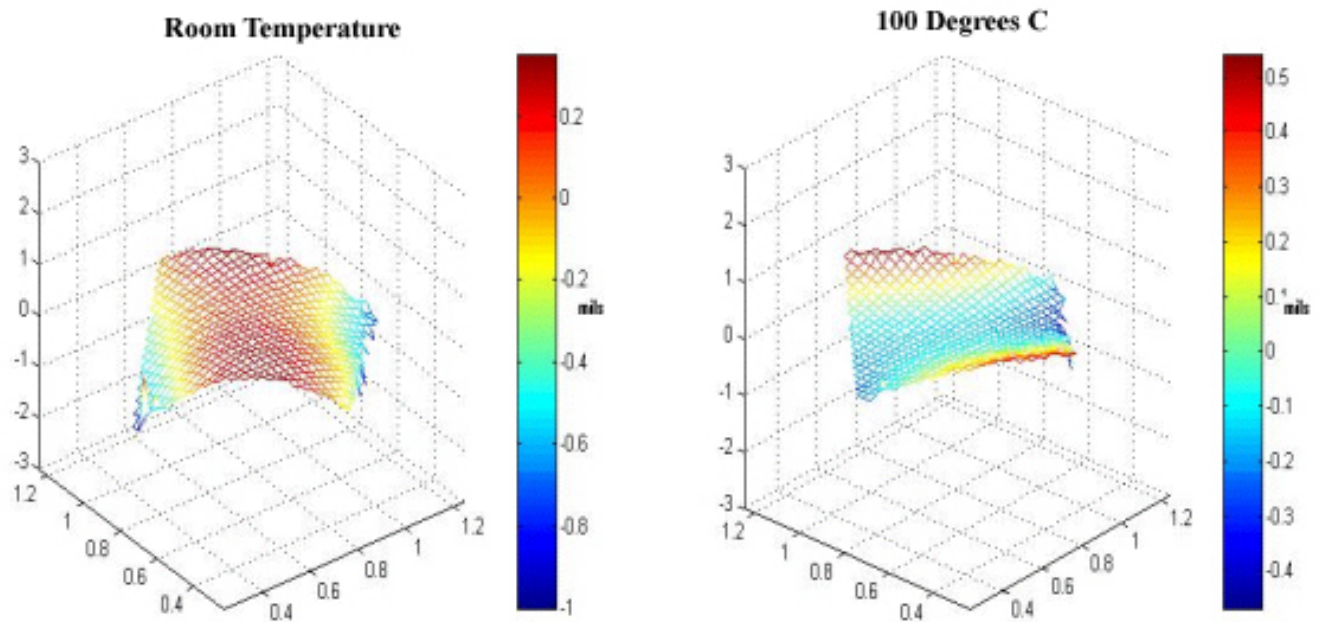
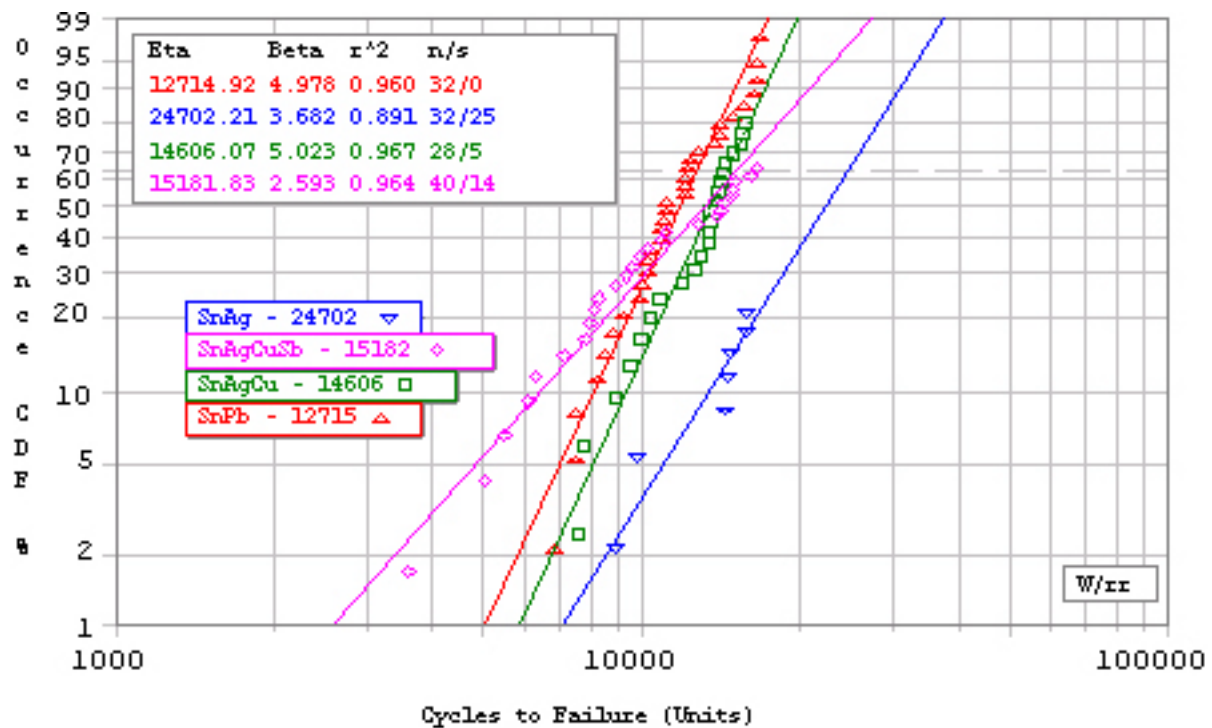**Figure 5 – Images Produced with Shadow-Moiré Interferometry of Delaminated Component (Ball Side Up)**

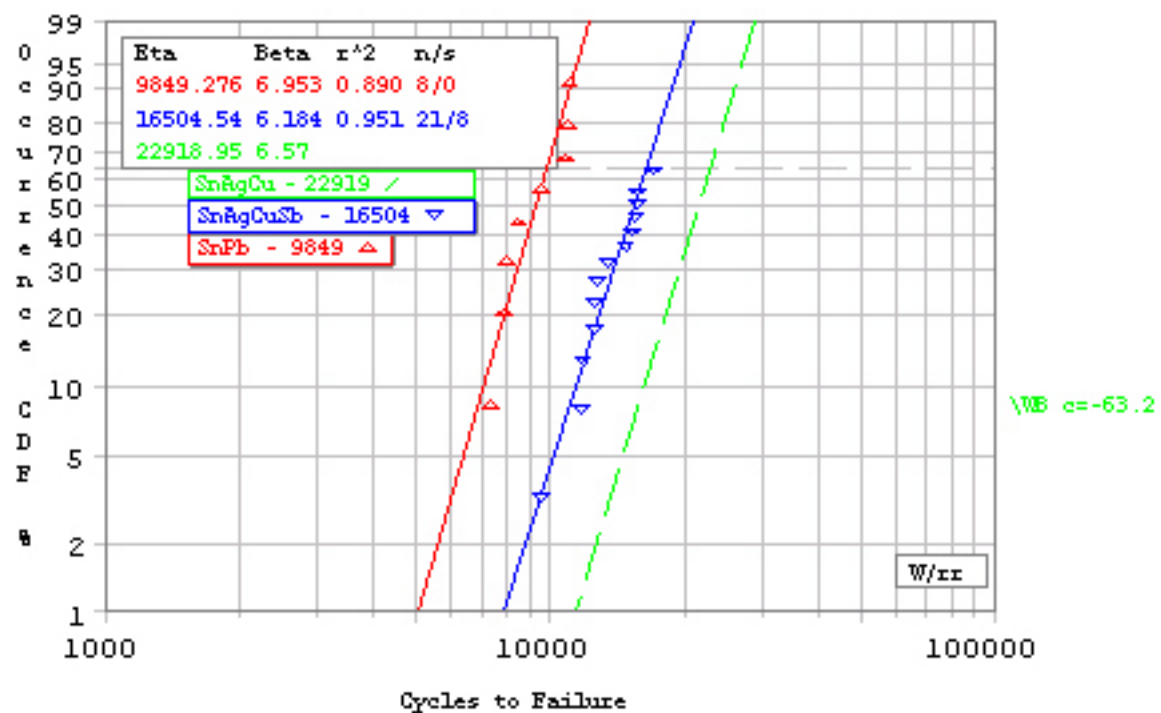**Figure 9 – Weibull Plot of TG1 Data Accumulated on ENIG PCBs**

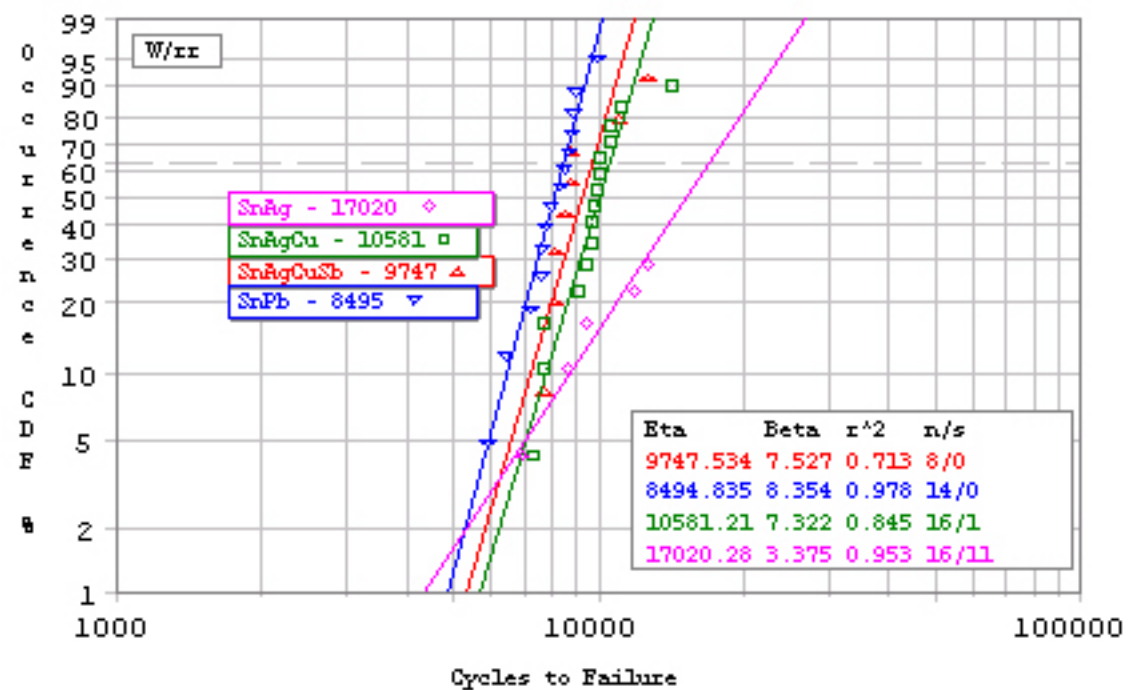**Figure 10 – Weibull Plot of TG1 Data Accumulated on Copper OSP PCBs**

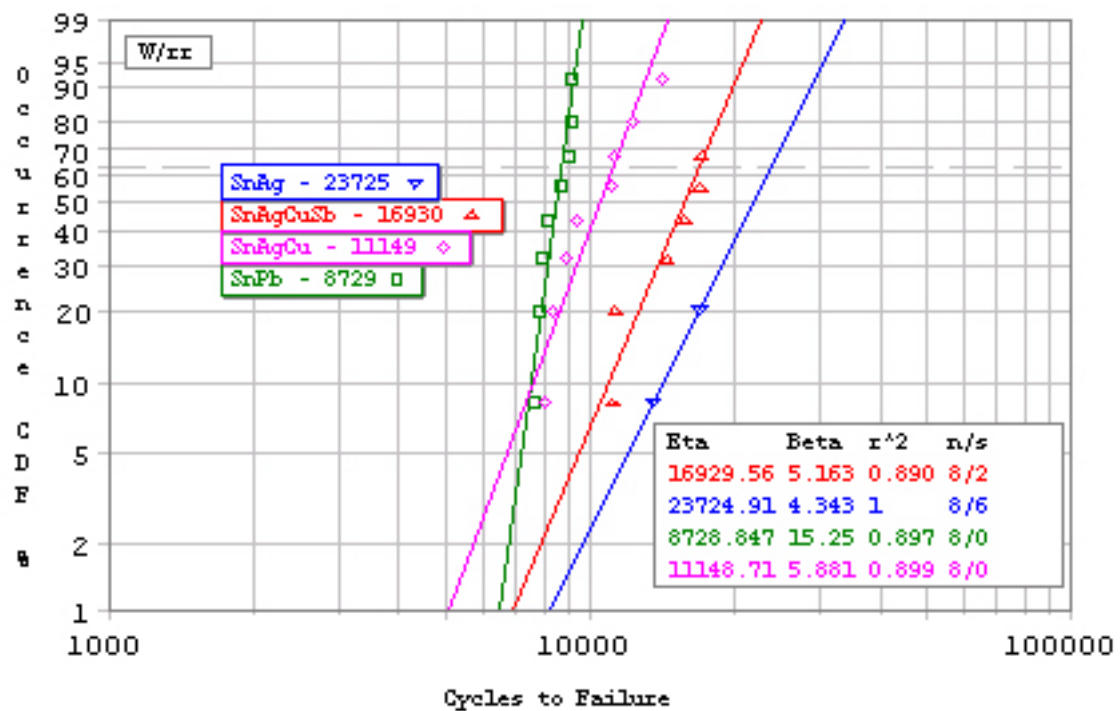

Figure 11 – Weibull Plot of TG2 Data Accumulated on ENIG PCBs

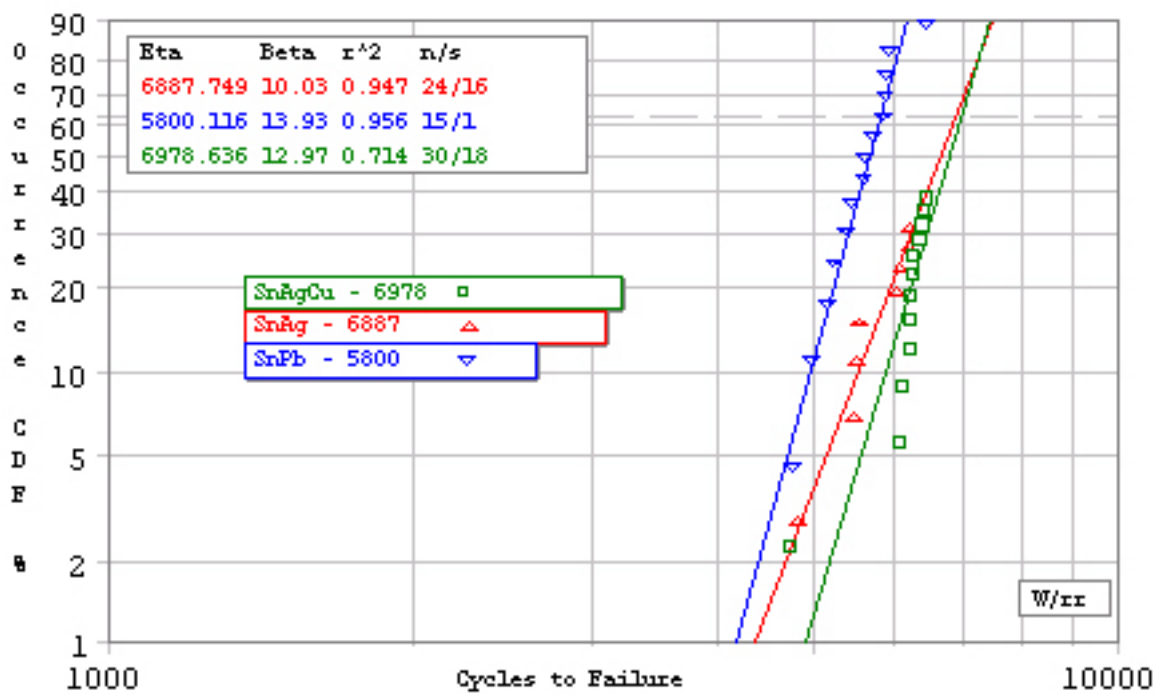**Figure 12 – Weibull Plot of TG2 Data Accumulated on OSP PCBs**

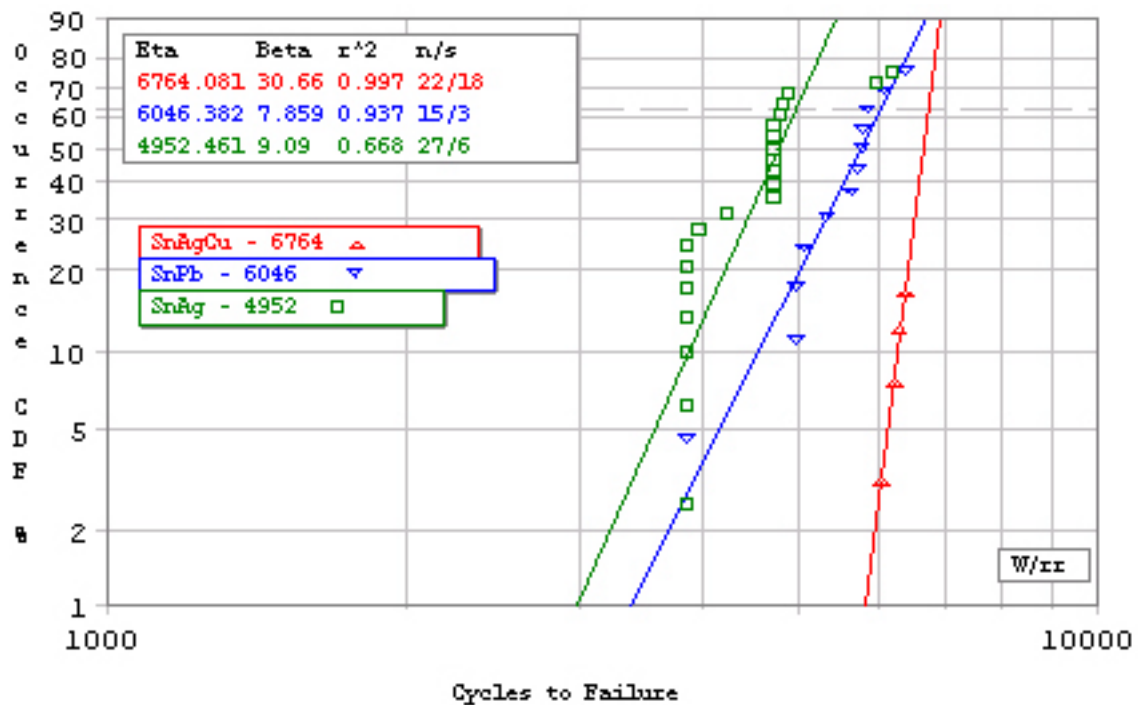**Figure 13 – Weibull Plot of –40/125°C Data Accumulated on OSP PCBs**

Figure 14 – Weibull Plot of –40/125°C Data Accumulated on ENIG PCBs

Solder	Solder Composition	Base Metal	Intermetallic Reflowed Thickness	Intermetallic thickness (Aging) Microinch	Aging Conditions	Ref.
Sn-Bi-In	17/57/26	Cu	Cu-Sn 35*	80	60C 500 hrs	22
Sn-Bi	42/58	Cu	Cu-Sn 40*	35	60C 500 hrs	22
Sn-Bi-In	17/57/26	Ni	Ni-Sn 5*	10	60C 500 hrs	22
Sn-Bi	42/58	Ni	Ni-Sn 5*	10	60C 500 hrs	22
Sn-Bi	42/58	Cu	Cu-Sn 40*	140	115C 500 hrs	22
Sn-Bi	42/58	Ni	Ni-Sn 5*	40	115C 500 hrs	22
Sn-Pb	63/37	Cu	Cu-Sn 55*	20	60C 500 hrs	22
Sn-Pb	63/37	Cu	Cu-Sn 55*	80	115C 500 hrs	22
Sn-Pb	63/37	Ni	Ni-Sn 5*	30	115C 500 hrs	22
Sn-Ag	97/3	Cu	Cu-Sn^	60	135C 12 hrs	23
Sn-Ag	96.5/3.5	Ni	Ni-Sn 40	80	125C 400 hrs	24
Sn-Ag	96.5/3.5	Ni	Ni_3Sn_4 40	100	125C 900 hrs	24
Sn-Ag	96.5/3.5	Ni	Ni_3Sn_4 40	125	150C 900 hrs	24
Sn-Ag	96.5/3.5	Ni	Ni_3Sn_4 40	135	160C 900 hrs	25
Sn	100	Ni	Ni_3Sn_4 35	260	160C 900 hrs	25
Sn-Pb	63/37	Ni	Ni_3Sn_4 10	100	160C 900 hrs	25
Sn-Ag-Cu-Sb	95.2/2.5/.8/.5	Cu	Cu-Sn 100	200	125C 750 hrs	X
Sn-Ag-Cu	95.5/3.8/.7	Ni	Ni-Sn+Cu-Sn	150	9,700 cycles 0-100C	X
Sn-Ag-Cu	95.5/3.8/.7	Ni	Ni-Sn+Cu-Sn	175	13,000 cycles 0-100C	X
Sn-Ag	96.5/3.5	Ni	Ni_3Sn_4 50	160	125C 750 hrs	X

*- 300 second liquid soak, ^ plated sample, #38 seconds above liquidus, X-data from this research paper TG1

Table 6 – Comparison of Intermetallic Thickness Values